Energy-saving discharge needle shape for electrohydrodynamic airflow generation

Donato Rubinetti [a,b,*], Kamran Iranshahi [a,c], Daniel I. Onwude [a], Bart M. Nicolaï [b], Lei Xie [d], Thijs Defraeye [a,e,**]

[a] *Empa, Swiss Federal Laboratories for Materials Science and Technology, Laboratory for Biomimetic Membranes and Textiles, Lerchenfeldstrasse 5, CH-9014, St. Gallen, Switzerland*
[b] *KU Leuven, BIOSYST-MeBioS, Willem de Croylaan 42, Heverlee, Belgium*
[c] *ETH-Zurich, Swiss Federal Institute of Technology, Zurich, 8092, Switzerland*
[d] *Belimed AG, Grienbachstrasse 11, CH-6300, Zug, Switzerland*
[e] *Food Quality and Design, Wageningen University & Research, P.O. Box 17, 6700 AA, Wageningen, the Netherlands*

ARTICLE INFO

ABSTRACT

Electrohydrodynamics (EHD) is a way to produce low energy-consuming airflow without moving components. The basis of airflow by EHD is corona discharge. A way to generate corona discharge is done, among others, via needle-type emitter electrodes whose shape and arrangement play a crucial role in the effectiveness of the discharge. Until now, the needle shape was chosen somewhat arbitrarily, although it impacts the energy consumption of the EHD process. We lack systematic studies on the impact of needle shape on the EHD discharge process and associated airflow to help engineers and scientists choose the best shape. This in-silico study screens the impact of the needle shape parameters on EHD performance in terms of electrical power consumption and airflow generation. The study aims to find the ideal EHD needle shape for unrestricted and confined flow. For this purpose, we test three different geometrical configurations. The first configuration is a free-flow single-needle configuration. The second configuration adds a dielectric nearby, which represents a needle enclosure. Lastly, a configuration including a dielectric and a converging nozzle is examined. All studies use a 2D-axisymmetric, fully automated EHD physics-based model. The first set of parametric studies explores the inherent geometrical properties of the needle shape, like tip radii (10–250 μm), needle cone angle (10–70°), and needle diameters (0.5–2 mm). The second set of parametric studies investigates the operation conditions, such as the emitter-collector distance (10–40 mm), the nozzle contraction ratio (0.04–1), and the operating voltage (6–32 kV). The results of the free-flow configuration show qualitative agreement with experiments on existing needle products. The ideal energy-saving needle shape for free flow configuration features a short conical tip length (i.e., a large angle $\geq 30°$), a diameter of 2 mm, and a needle rip radius of 100 μm. The situation changes when a dielectric is present, and a sharp angle of 10° is favorable to reduce energy consumption. Since a dielectric inverts the optimal needle shape, it makes sense to customize it for a particular application in EHD airflow generation. We provide performance maps that can be used as design charts. This study is a guideline to optimize EHD devices further to reduce energy consumption and increase airflow speed.

1. Introduction

Electrohydrodynamics (EHD) can produce low energy-consuming airflow in a solid-state fashion without moving components. EHD is based on corona discharge, producing ions out of air molecules that accelerate in a strong electric field between the emitter electrode (producing ions) and collector electrode (collecting ions). In transition, the air ions exchange momentum with surrounding neutral air molecules. A

---

macroscopic airflow, or ionic wind, emerges [1]. EHD has intriguing applications in alternative airflow propulsion systems [2], where it has the potential to reduce noise emissions and energy consumption substantially [3]. Moreover, ionic wind can, among numerous applications, be used for air purification [4], convective cooling [5,6], improving heat transfer [7], and airflow control [8]. EHD is an exciting contender for other low-energy airflow generators as it can be scaled to miniature size and needs as little as a few μA of electric current.

There is no generic design for EHD airflow generators, sometimes called EHD air movers or ionic wind accelerators [9]. Especially different arrangements of the emitter and collector electrode have been extensively researched to enhance EHD-generated airflow with the least current possible [10]. For the emitter, the most prominent shapes are wire or needle electrodes [11]. Needles are handy for maintaining a continuous, stable discharge and a more extensive operation range [12]. The needle emitter shape also significantly impacts the characteristics of the ionic wind [13]. Experimental studies on the optimization of electrodes are often accompanied by simulation work to visualize electric fields and spot further optimization potential [14]. The produced ions should propagate in the direction of the intended airflow stream to maximize convective momentum transfer. The momentum transfer occurs on the electric field lines, which are strongly defined by the shape and arrangement of emitter and collector electrodes [15]. Despite its significance, research on the effect of the needle emitter geometry on electrical and aerodynamic performance is limited. However, present work in this field has yielded some encouraging results [13,16–18].

We want to understand how the shape of the needle affects airflow in free flow and confined flow and how much electrical energy is used. For this purpose, we study three different configurations: #1 free flow, #2 constrained flow with nearby dielectric, and #3 when a converging nozzle is introduced. Configurations #2 and #3 are attractive, e.g., for miniaturized EHD airflow devices [19], where the needle is placed within an enclosure. An enclosure with the ionizing needle within is typically a non-conductive material acting as a dielectric which alters the electric field lines [20]. A nearby dielectric is one of the influencing factors for EHD-generated airflow. Many other factors, such as polarity, number of emitters, electrode arrangement, and sequential staging of EHD units, have been investigated to date [21], mostly experimentally. Adopting a broad view of how needle shapes affect airflow is essential. Custom-made needles are quickly produced and can make a distinct difference in energy consumption and convection. However, experimentally studying several needle angles, needle diameters, and needle tip radii under different conditions requires many samples and resources.

We adopt a fully coupled numerical physics-based model to evaluate the performance of different needle configurations for this study regarding energy consumption and airflow characteristics. We run the simulations in a 2D-axisymmetric manner with a Lagrange multiplier procedure that automatically evaluates the current density on the electrode as we alter the shape of the needle for every configuration [20]. Our fully coupled model allows a thorough scan of the design space. For validation purposes, we compare our results with experimental data.

2. Materials and methods

The simulation strategy is intended to study the needle design parameters such as needle tip radius, needle tip angle and diameter, and needle-ground electrode distance. The results are compared to experimental data of common needle types [13]. We quantify the results in average outflow speed, electric power consumption, and transduction efficiency. The latter metric is the ratio of airflow rate to power consumption. All results are normalized with the maximum calculated value of the respective configuration to ensure cross-comparison within and between configurations. Our simulations are performed using a two-dimensional axisymmetric model. The model accounts for corona

discharge (electrostatics) and laminar airflow (computational fluid dynamics, CFD) in a fully coupled manner. The discharge within the air domain is represented as a continuum, i.e., a single-species approach where the ionized air fraction consists of air with a non-zero charge [22–24]. This section describes the boundary conditions, simulation settings, and assumptions of the single-species approach.

2.1. Computational system configuration

Fig. 1 gives an overview of all investigated 2D-axisymmetric configurations. The red highlighted boundary is the ground boundary (collector), while the voltage boundary condition is applied all over the needle.

Configuration #1 is the free flow single needle case where the needle tip and grounded electrode have an inter-electrode distance δ [mm]. In this configuration, we intend to isolate the effects of the needle shape on airflow dynamics by excluding the influence of other geometrical or physical parameters. The grounded electrode boundary, a wire mesh or another complex structure, is a simple plane in the fluid flow model outlet. We recognize that this simplification may not accurately depict real-world scenarios. However, it enables us to focus solely on the influence of needle shape. The outlet has zero static pressure and permits the flow to pass. On the left side is the inlet boundary, where air flows in with zero total pressure. The upper boundary acts as a no-slip wall. The 50 mm distance between the needle and the wall is chosen so that the wall impacts airflow development the least.

Configuration #2 is similar to the first configuration but with a dielectric introduced at a distance of 5 mm from the needle axis. With a distance of 5 mm, we allow enough airflow to pass through while ensuring a measurable impact of the dielectric. The dielectric separates the air domain Ω_{air} into three subdomains $\omega_{air,1}$, $\omega_{air,2}$ and $\omega_{dielectric}$. The convective airflow is expected to occur in the subdomain $\omega_{air,2}$ while in $\omega_{air,1}$ we predict the airflow to be zero. Nonetheless, this non-moving air subdomain $\omega_{air,1}$ remains crucial as it is affected by the electric field, including the distortion of electric field lines by the dielectric. This electric field influence affects the transport of charges in the airflow subdomain $\omega_{air,2}$. Here, the outlet is also reduced to the same height as the air domain $\omega_{air,2}$, but the ground is applied throughout the right boundary. It is necessary to maintain the same ground to compare the electric performance of the needle with configuration #1, as we want to know the impact of the introduced dielectric. The electrostatic part of the model acts over all subdomains. In particular, the dielectric with an assumed relative permittivity of $\varepsilon_r = 3$ of is expected to distort the electric field considerably [20,25].

The last configuration, #3, shows the case when we introduce a nozzle in a more extended domain. Here, the grounded collector electrode is placed directly onto the nozzle walls. Introducing this nozzle is relevant to studying the effect of flow contraction, i.e., when we submit EHD-convection to a pressure-decreasing and velocity-increasing aerodynamic entity. We assess various contraction ratios of the nozzle. This configuration is exciting for cases where EHD convection devices shall be designed which achieve higher airspeeds than regular EHD free flow devices [19]. An example is the EHD air amplifier which combines EHD airflow with a Coanda surface that requires a high-speed EHD jet [20].

2.2. Physics-based modeling

A fully coupled corona discharge – computational fluid dynamics (CFD) model is adopted, effectively using computational resources. The approach has been described thoroughly in [20]. In a single study step, it calculates the three governing equations (Poisson's, charge transport, and Navier-Stokes). Previous research on the matter has been conducted primarily on a step-wise approach [22,24,26,27]. To accommodate the model in a solver-friendly mathematical description, auxiliary equations are necessary and described in the following.
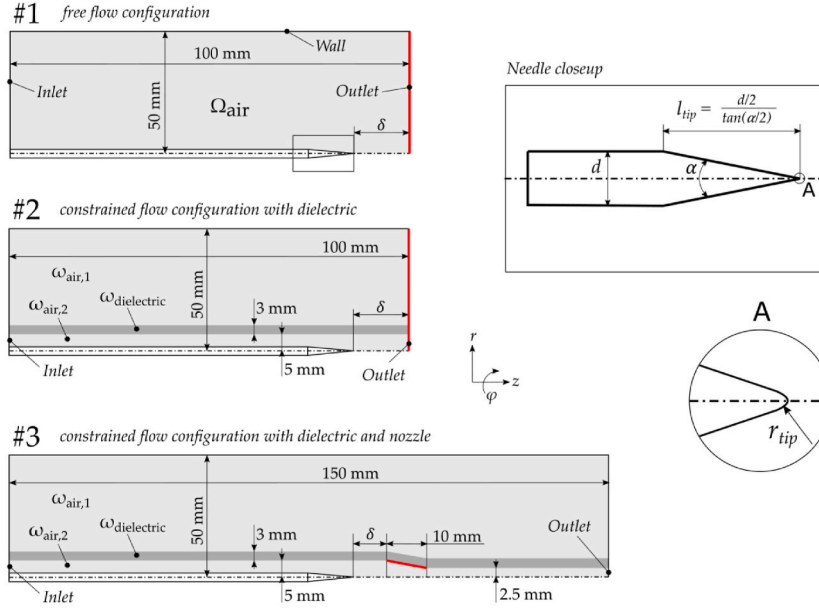
Fig. 1. Configurations used in the simulations where #1 is the free flow configuration without dielectric, #2 is the constrained flow configuration with dielectric, and #3 is the configuration with dielectric with nozzle and contraction ratio 0.25. The boundaries highlighted in red are the collectors, e.g., the ground boundary conditions.

2.2.1. Electrostatics

EHD airflow can be divided into an electrostatic part for the corona discharge and a fluid flow part for the airflow. As for the electrostatic part, we need Poisson's Equation (1) and the charge transport Equation (2).

$$\nabla^2 \varphi = -\frac{\rho_{el}}{\varepsilon_0 \varepsilon_r} \tag{1}$$

$$\nabla \bullet (\rho_{el} b \boldsymbol{E} + \rho_{el} \boldsymbol{u} - D_{ion} \nabla \rho_{el}) = 0 \tag{2}$$

In Equation (1), the dependent variable is the electric potential φ [V]. There we also find the space charge density ρ_{el} [C m^{-3}] as well as the vacuum permittivity ε_0 and the relative permittivity ε_r (in air, $\varepsilon_r = 1$). In Equation (2), the dependent variable is the space charge density. b describes the ion mobility (in air, 1.8×10^{-4} m^2 V^{-1} s^{-1}). The electric field vector $\boldsymbol{E}$ can also conveniently be expressed as a gradient of the electric potential $\boldsymbol{E} = -\nabla \varphi$, thus allowing for a stronger coupling between Equations (1) and (2). $\boldsymbol{u}$ [m s^{-1}] is the air velocity vector accounting for external convection sources and D_{ion} [m^2 s^{-1}] is the ion diffusivity. Often, the external convection term and the diffusivity term in Equation (2) are neglected as the first term $\rho_{el} b \boldsymbol{E}$ is several orders of magnitudes larger [5,28]. We omit the external convection term but include the diffusive term $D_{ion} \nabla \rho_{el}$ despite its vanishing physical contribution as it shows to improve numerical stability.

For Poisson's Equation (1), two Dirichlet-type boundary conditions specifying the voltage are sufficient. For the space charge transport equation, we need one boundary condition accounting for the space charge on the needle electrode. The definition of this boundary condition is complex because the space charge on the needle electrode is not constant over the boundary surface. Only the areas exceeding a specific electric field value E_0 [V m^{-1}] produce ions and, hence, charge. A commonly accepted empirical value for the corona discharge electric field strength E_0 for needle electrodes is the Peek-Kaptzov condition [29]

$$E_0 = 3.1 \left[\text{V m}^{-1} \right] \bullet 10^6 \bullet \left(1 + \frac{0.308}{\sqrt{0.5 \bullet r_{tip}[\text{cm}^{-1}]}} \right) \tag{3}$$

where r_{tip} [m] is the tip curvature radius of the needle electrode. To ensure that charge is produced only on the needle areas where the value of E_0 is reached, we impose a weak constraint on the needle boundary. To do so, we remove the strict voltage boundary condition for electric potential on the needle and replace it with a weak expression

$$0 = (\varphi_0 - \varphi) \tag{4}$$

where φ_0 is the target voltage for the needle, and φ is the dependent variable for Poisson's Equation. In that way, we introduce a new variable λ which corresponds to the space charge density boundary condition on the electrode. Additionally, we add also an electric displacement field $\boldsymbol{D_0}$ [C m^{-2}] boundary condition on the needle boundary to account for the corona discharge onset field strength

$$\boldsymbol{D_0} = [0 \quad -\varepsilon_0 E_{local}]^\text{T}. \tag{5}$$

Here, $\boldsymbol{D_0}$ is a vector parallel to the boundary normal. E_{local} [V m^{-1}] is a variable tracking the current value of the electric field on the needle, where the electric field is strongly non-uniform. E_{local} has the values

$$E_{local} = \begin{cases} |-\nabla\varphi| & , |-\nabla\varphi| < E_0 \\ E_0 & , |-\nabla\varphi| \geq E_0 \end{cases} \tag{6}$$

which means that on the needle electrode, the electric field varies depending on location and needle shape as well as applied voltage. That way, irrespective of needle shape, we can predict the areas where the boundary is actively ionizing the surrounding air.

2.2.2. Airflow model

The airflow model is given by the Navier-Stokes momentum Equation (7) and the continuity Equation (8)

$$\rho \boldsymbol{u} \bullet \nabla \boldsymbol{u} = -\nabla p + \mu \nabla^2 \boldsymbol{u} + \rho_{el} \boldsymbol{E} \tag{7}$$

$$\rho \nabla \bullet \boldsymbol{u} = 0 \tag{8}$$

where ρ [kg m^{-3}] is the air density ($\rho = 1.2$ kg m^{-3}), $\boldsymbol{u}$ [m s^{-1}] is the velocity field. p [Pa] is the pressure, and μ [Pa s] denotes the dynamic viscosity of air ($\mu = 1.81 \bullet 10^{-5}$ Pa s). Note that the momentum equation features an additional volume force term $\rho_{el}\boldsymbol{E}$, which represents the Coulomb force as the driving force of charge migration between

electrodes. Given the dimensions of the configurations and velocities <1 m s^{-1}, resulting in a Reynolds number of 662 or less, it is safe to assume laminar flow conditions.

2.3. Numerical simulation runs and implementation

Table 1 lists all simulation runs during the investigation of the design space of a needle in the three suggested configurations. The first simulation is a validation study where we prove the model's validity by comparing the model results to experimental data. The details of the validation case are given in the following section. Then, a benchmark case is run where four common needle types (machine sewing needle, thin pin, hand sewing needle, construction nail) are studied and compared to experimental data [13]. The base case voltage is set to 14 kV, corresponding to the measured breakdown voltage for the construction nail [13]. This voltage value is kept constant until the last simulation to ensure cross-comparison between the configurations.

The challenging part of modeling EHD airflow is determining the emitter electrode's space charge density. A priori, it is unknown which part of the needle electrode "burns," i.e., can ionize its surroundings. This inherent problem with modeling EHD airflow makes it particularly difficult to study the corona discharge properties of needle geometries.

The physics-based EHD model is built within COMSOL Multiphysics version 6.0, a commercial finite element solver. The electrostatic and airflow models are calculated and solved simultaneously. The modules used in this model are "Electrostatics," "Coefficient Form PDE," and "Laminar Flow." The parameter combinations for each file are included via a "Parametric Sweep" study node. The solver is MUMPS (Multifrontal Massively Parallel sparse direct Solver) in combination with linear shape functions. For computational fluid dynamics (CFD), the chosen solver is PARDISO (PARalel Direct sparse solver), a segregated solver with quadratic shape functions. Additionally, the solver was set to store NaN (Not-a-Number) solutions wherever convergence is not achieved to observe the limits of the design space.

We conducted a mesh sensitivity analysis in a previous study with Richardson extrapolation [20]. The maximum error from the exact solution is 2.1 % for the speed. In this model, we adopt the same strategy resulting in a mesh with 23,735 elements for the free flow configuration. The configuration with dielectric contains 19,565 elements, and the nozzle configuration contains 24,796 elements. The elements are mixed and refined in proximity to the needle tip.

2.4. Validation experiments and model

2.4.1. Test rig

Figs. 2 and 3 depict the test rig setup used to generate experimental data to validate the numerical model. The design consists of three different tubes forming an extended tunnel. Each tube is 200 mm long and measures 75–80 mm in diameter. The middle section is an aluminum tube that functions as the collector. In contrast, the PVC tubes at the beginning and the end form the inlet and outlet sections acting as flow straighteners. Due to the inherent dangers of high-voltage experimentation, the entire apparatus is enclosed within a $1 \times 1 \times 2$ m^3 high-voltage safety environment that also functions as a Faraday cage to prevent electromagnetic interference. External to the safety enclosure, the needle emitter-collector arrangement is connected to a high-voltage power supply. The electric current can be measured directly from the DC high voltage supply Spellmann SL30PN10 (Spellman High Voltage Electronics Corporation, 475 Wireless Blvd, Hauppauge, NY 11788).

For the airflow measurement, we use a calibrated Testo 405i hot-wire anemometer (Testo SE & Co. KgaA, Celsiusstrasse 2, 79,822 Titisee-Neustadt. Accuracy $\pm$ 0.1 m s^{-1}, Resolution 0.01 m s^{-1}, Measuring time interval 1 s). In order to perform point measurements in multiple locations of the tube, the rear flow stabilizer has apertures to accommodate the sliding hot-wire anemometer. The anemometer is attached to a linear guide propelled by an electric motor, allowing it to travel at a constant speed. This configuration allows for precise velocity profile recordings with an accuracy of 1 mm per second. This apparatus offers the necessary control and measurement precision for validating the proposed numerical modeling strategy.

The laboratory temperature and humidity conditions are monitored with a Sensirion SHT31 sensor (SENSIRION AG, Laubisruetistrasse 50, 8712 Staefa, Switzerland. Accuracy on humidity $\pm$ 1.5 % and $\pm$ 0.1 °C on temperature). Each experimental data point is replicated three times, and the result is expressed as average $\pm$ standard error.
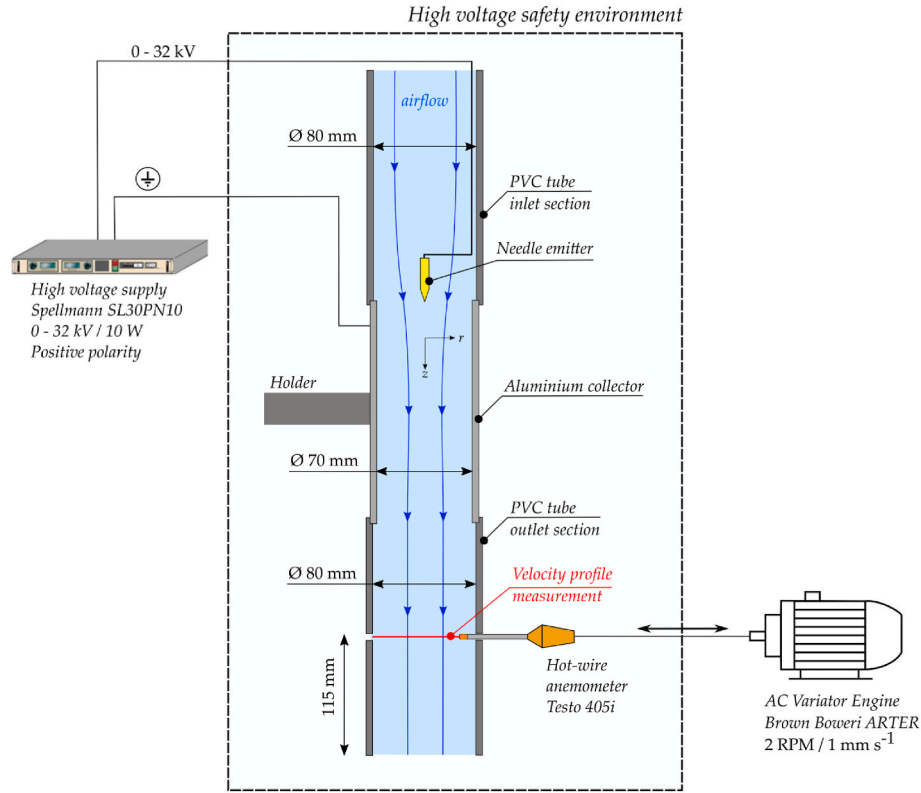
2.4.2. Numerical model

The experimental setup geometry is simplified to a 2D-axisymmetric geometry to accommodate the numerical model. Fig. 4 shows the numerical model setup, including exact dimensions, boundary conditions, and measurement (evaluation) locations. The modeling, meshing, and evaluation procedures are analogous to the previous sections. Given the dimensions of the tubes, the airflow model is adapted using a $k - \varepsilon$ turbulence model, as the Reynolds number is expected to be above approximately 5300. The $k - \varepsilon$ model was specifically selected due to its stability and efficacy in demonstrating EHD-driven flows [30].

Table 1
Numerical model list for every configuration and parameter setting.

Name	Description/ Configuration	Needle distance	Needle tip angle	Needle body diameter	Needle tip radius	Nozzle gap size	Needle voltage	Number of simulations
		δ [mm]	α [°]	d [mm]	r_{tip} [μm]	ε [mm]	φ_0 [kV]	No. [−]
a_validation	Validation case	n/a	43.6	6	40	n/a	6–32	14
a_benchmark	Benchmark case [13]	20	14–30	0.32–2	80–250	n/a	14	4
a_param_20	Free flow #1	20	10–70	0.5–2	10–250	n/a	14	140
b_param_20	Dielectric #2	20	10–70	0.5–2	10–250	n/a	14	140
b_param_30	Dielectric #2	30	10–70	0.5–2	10–250	n/a	14	140
b_param_40	Dielectric #2	40	10–70	0.5–2	10–250	n/a	14	140
c_param_20	Dielectric and nozzle #3	20	10–70	0.5–2	10–250	2.5	14	140
c_param_30	Dielectric and nozzle #3	30	10–70	0.5–2	10–250	2.5	14	140
c_param_40	Dielectric and nozzle #3	40	10–70	0.5–2	10–250	2.5	14	140
c_epsilon_20	Dielectric and nozzle #3	20	10	2	100	1–5	14	17
c_voltage_10	Dielectric and nozzle #3	10	10–70	2	100	3.5	6–32	98

Fig. 2. Experimental test rig for retrieving experimental data to validate the numerical modeling approach. The airflow acceleration occurs in the middle section where the needle emitter and aluminum collector are connected to the DC high-voltage power supply with variable voltage. Before and after the middle section, two PVC tubes are attached, acting as flow straighteners. In the outlet section, the tube has perforations allowing a hot-wire anemometer to slide through. It records a data point every second and measures the velocity profile.
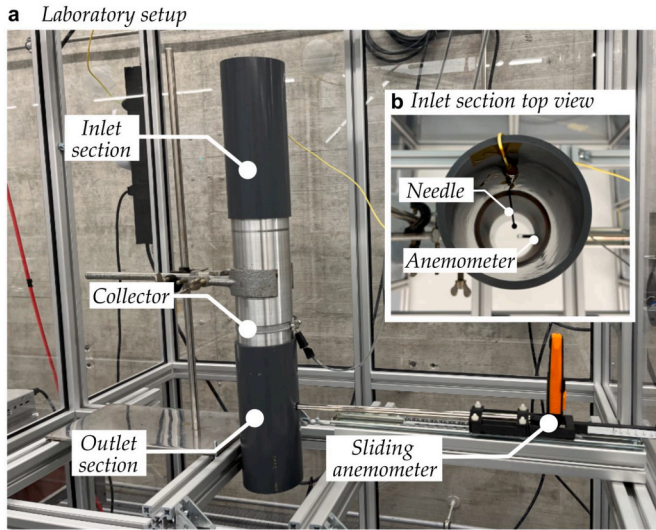
Fig. 3. Photograph of the experimental test rig with main components marked. Subfigure (a) shows the interior of the high voltage safety environment where the entire tube is suspended. On the right side, the anemometer is mounted on a linear guide to slide the probe in and out of the outlet section. This allows for a precise measurement of the velocity profile downstream. Subfigure (b) is the top view of the inlet section showing the needle and anemometer.

2.5. Performance evaluation metrics

We evaluate the performance of each needle shape parameter set based on metrics such as outlet speed, electric power consumption, and transduction efficiency. For the average outlet velocity magnitude $\bar{u}_{out}$ [m s^{-1}], we integrate the velocity magnitude u [m s^{-1}] over the respective outlet boundary s [m] of each configuration and divide by boundary length section l_s [m].

$$\bar{u}_{out} = \frac{1}{l_s} \int_0^{l_s} u \, ds. \qquad (9)$$

For configuration #1, the outlet boundary section length is $l_s = 50$ mm. For configuration #2, l_s equals 5 mm, corresponding to the subdomain $\omega_{air,2}$ outlet boundary. For configuration #3, the length is variable, $l_s = \varepsilon$.

For electric power consumption P_{el} [W] we calculate

$$P_{el} = I \bullet \varphi_0 \qquad (10)$$

where the needle electrode voltage is φ_0 [V] and I [A] is the electric current derived from surface integration of the current density $\rho_{el} b |E|$ on the needle boundary s [m] and then multiplied by the needle surface A_{needle} [m^2].

$$I = A_{needle} \int_{needle} \rho_{el} b |E| \, ds. \qquad (11)$$

The last metric is the transduction efficiency γ [m^3 s^{-1} W] as a measure for the flow generated per electrical power invested. Ideally, we achieve the highest airspeed parallel to the needle axis. However, depending on the needle electrode's shape and the electric field variations, the velocity component perpendicular to the needle axis may create a cross-flow effect that decelerates the parallel velocity component. The shape of the needle solely causes this effect and can quickly be addressed constructively. That gives importance to the transduction efficiency as a value that assesses the inherent performance of the needle to generate flow most efficiently. We define transduction efficiency as
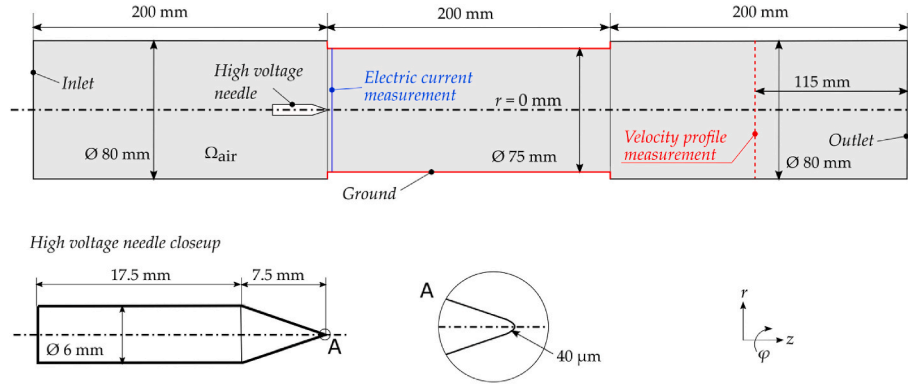
Fig. 4. Numerical setup for the experimental validation of our physics-based model. The tube-like geometry is simplified to a 2D-axisymmetric arrangement. The modeling and meshing procedure follows the description in Sections 2.2 and 2.3.

$$\gamma = \frac{\overline{u}_{out}}{P_{el}}. \tag{12}$$

These three key metrics given by Equations (9), (10) and (12) are normalized during evaluation. We normalize the absolute values with the maximum attained value within the comparison group for better comparison across the different needle shapes and types.
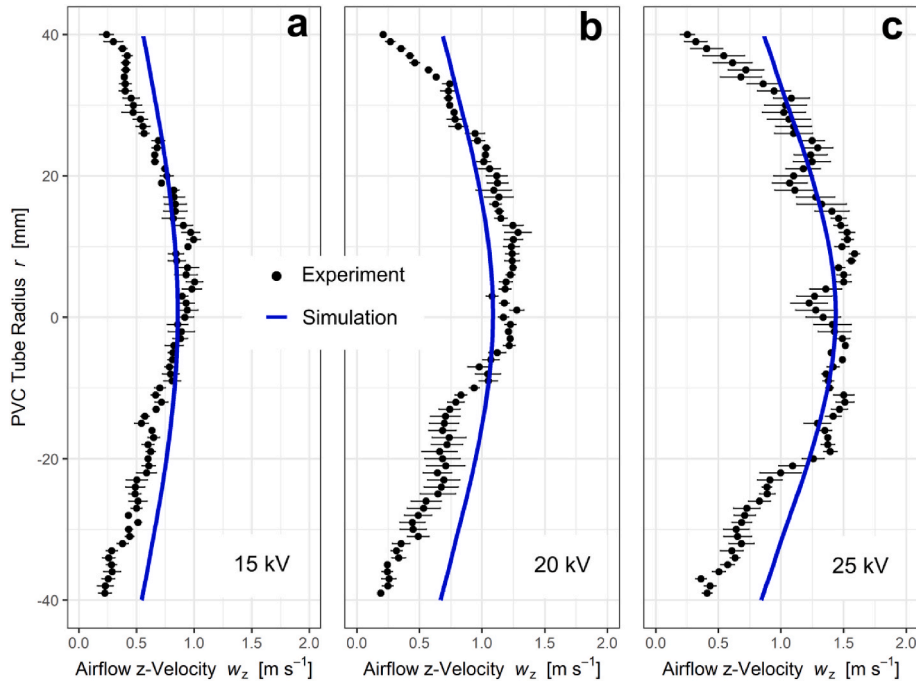
3. Results

3.1. Validation of the numerical modeling approach

This section thoroughly compares experimental data and our 2D-axisymmetric numerical model built for validation. Fig. 5 compares the velocity profiles for 15, 20, and 25 kV voltage levels. It is evident that the simulation results correspond reasonably well with the experimental results. However, an interesting finding is that the simulation results consistently underpredict the airflow velocity at the PVC tube's walls at $r = \pm 40$ mm. This observation can be attributed to several factors, but most likely to the limitations of the turbulence model near the wall, and

requires further investigation.

Fig. 6 illustrates the CFD airflow results for the flow field and streamlines of our test rig validation case. The velocity maps are displayed for 15, 20, and 25 kV. These visualizations provide a direct comparison of the actual airflow behavior. The zone of highest acceleration is right downstream of the needle tip. At higher voltage levels, the high-speed zone is more extensive, which also causes the surrounding air to accelerate more. Near the corners of the middle section, we observe some recirculation zones in all cases.

Despite some observed discrepancies in the velocity profiles at near-wall locations, our experiments and simulations are in close agreement when evaluating integral quantities such as electric current and average airflow speed. As depicted in Fig. 7, these results demonstrate that discrepancies are predominantly localized, validating our overall modeling approach. Nonetheless, we observe more significant variations in electric current as voltage levels increase. Just below the breakdown voltage, at 26.5 kV, the continuous corona discharge transforms into an uncontrolled arc discharge. The transition from corona to arc discharge adds complexity not accounted for in our simulations.

Fig. 5. Comparison of the velocity profiles for voltage levels of 15 (a), 20 (b), and 25 kV (c). The simulation results correspond adequately with the experimental results. There is consistent underprediction in airflow at the walls of the PVC tube, i.e., at $r = \pm 40$ *mm*.
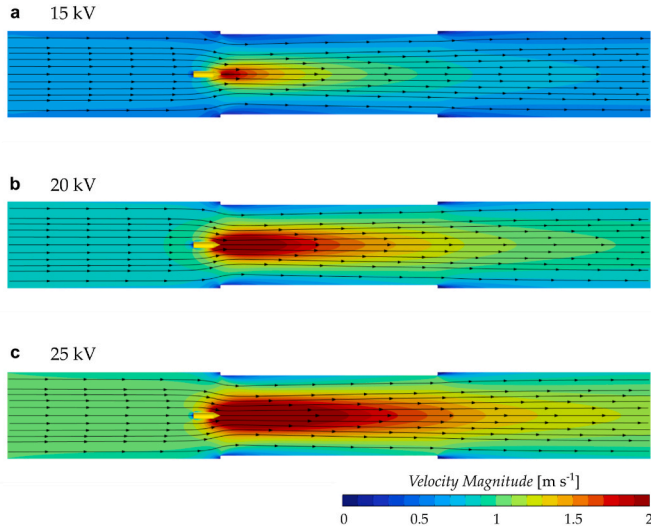
Fig. 6. CFD airflow results for the flow field and streamlines within the test rig validation case. The airflow behavior is displayed for the voltage levels 15 kV (a), 20 kV (b), and 25 kV (c).

3.2. Ideal needle shape for free flow configuration and comparison to commonly used needle electrodes

This section shows the results for the free flow configuration #1, which is the simplest configuration. The results for the needle body diameter $d = 2$ mm are reported in the performance maps in Fig. 8, as this diameter is the overall best performer in achieving a sustained discharge. We set the base case tip radius at $r_{tip} = 100 \, \mu$m which is a value that readily translates into reality from a manufacturing point of view. We could achieve such radii with a single production step in the workshop using an ordinary turning lathe. Radii larger than $100 \, \mu$m could be attained by grinding. Smaller radii require advanced manufacturing tools and expertise.

From Fig. 8a, we learn that the needle tip radius and the needle tip angle have little influence on the average outlet velocity magnitude. The value is measured at the outlet, which coincides with the grounded electrode boundary, according to Fig. 1a. Following CFD best practices, we also tested a prolonged geometry with an outlet further away from the grounded electrode boundary to assess the change in average velocity. When the ground and outlet are further apart by 50 mm additionally, the average velocity is up to 3.9 % higher. This value is

sufficiently small to justify our choice of boundary conditions for the comparative studies.

With the increasing angle of the needle tip, the velocity magnitude slightly decreases. We explain this effect with the needle's inherent properties, which modify the electric field lines. The electric field vector component perpendicular to the needle axis gains more importance with increasing angle. Therefore, if the needle is optimized for velocity only, a few % more airflow speed can be obtained using a sharp cone angle of 10°.

However, a sharp angle also increases the production of charges, leading to an overall increase in electric power consumption. With sharper angles, a more significant portion of the tip satisfies the Peek-Kaptzov condition, resulting in a larger surface area with an electric field strong enough to generate electrical charges. Supplementary Material A provides a more detailed evaluation of charge production. Contrary to general expectation [31], our findings in Fig. 8b show a slight decrease in discharge current and power consumption as r_{tip} descreases, particularly at sharp needle tip angles. This trend may stem from Peek's formula's inability to accurately represent extremely sharp needles [32].

According to Fig. 8b, doubling the cone angle from 10° to 20° already reduces the power consumption by 20 %. Looking at the normalized transduction efficiency, we observe that larger angles are preferable to reduce inefficiencies when generating more airflow with less energy input.

We can mainly influence the electric power consumption with the needle shape in the free flow configuration. The overall ideal needle shape has a diameter of $d = 2$ mm, a needle tip angle of $\alpha = 30°$, and a needle tip radius of $r_{tip} = 100 \, \mu$m. We compare the power consumption of the ideal needle to commonly available needle products in Fig. 9 with experimental data [13]. The machine sewing needle consumes most electrical power as it appears to ionize throughout its body, not just the needle tip. Our ideal needle tip is closest to the construction nail regarding power consumption. Previously, we could see that the needle tip radius plays a marginal role in airflow speed and energy consumption. This comparison shows that energy consumption depends strongly on the needle body diameter. We can create a more pronounced jet of charged air molecules by choosing a larger body diameter. This is because there are stronger asymmetries in the electric field when the tip is sharper than the body of the needle. Fig. 10 compares these common needle types' electric field lines emerging from the needle tip. We find that the needle diameter plays a significant role in spreading out the field lines from non-ionizing sections of the needles (cyan). In contrast, the ionizing tip maintains its field line density (magenta) regardless of
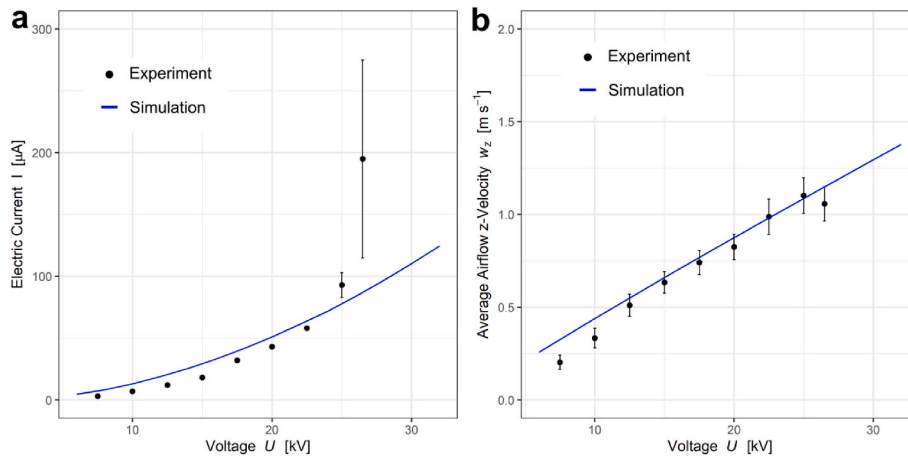
Fig. 7. Comparison of electric current (a) and average velocity (b) results for the simulation and experiments. There is good agreement between experiment and simulation. However, the experimental data is error-prone as the voltage approaches breakdown voltage at 25 kV. Beyond 26.5 kV, the continuous corona discharge turns into an uncontrolled arc discharge.
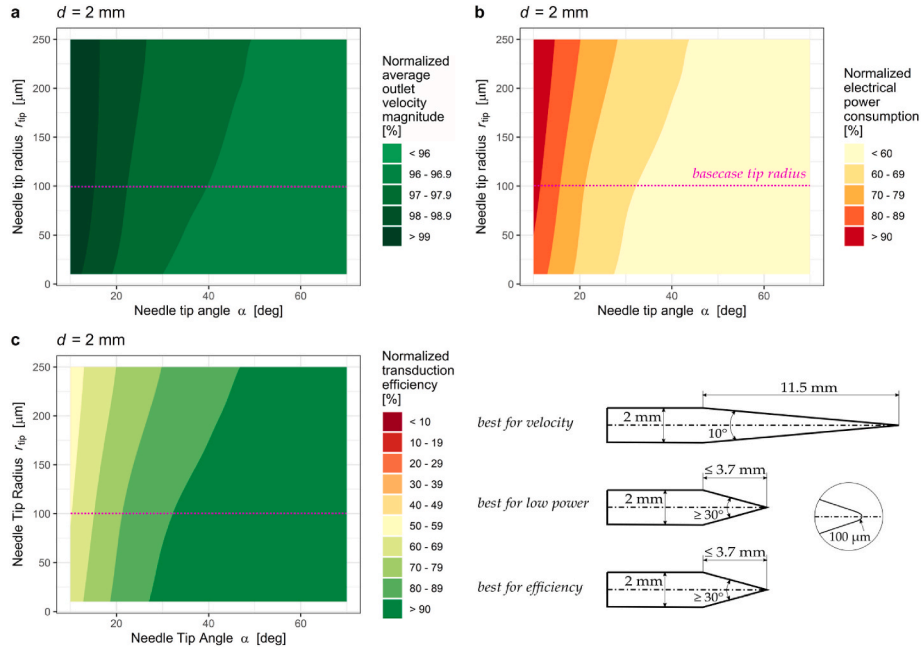
Fig. 8. Normalized velocity (a), power consumption (b), and transduction efficiency (c) maps for free flow needles as a function of needle tip radius and angle for the free flow configuration. The velocity magnitude is evaluated at the grounded boundary electrode, while the power consumption is evaluated at the electrode boundary. In free flow, the velocity magnitude seems less sensitive to needle tip radius and angle, implying that the electric field lines are well distributed in either parameter combination and little interference occurs during momentum transfer. A more considerable difference is observed in power consumption where the needle parameters increase or decrease the production of charges which directly translates to power consumption.

| d	[mm]	0.32-0.44	0.7	1.2	1.8	2
r_{tip}	[μm]	80	90	110	250	100
α	[°]	14	25	22	22	30
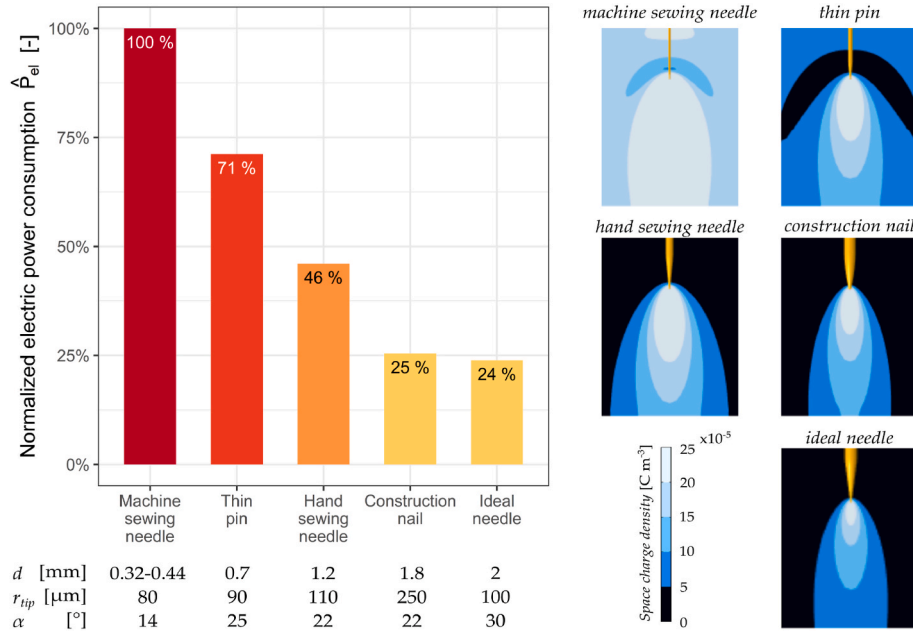
Fig. 9. Normalized electric power consumption of common needle types compared to the ideal needle calculated in the simulations [13]. The machine sewing needle is the reference as it uses the most electric power. With such a small body diameter, the tip and entire body tend to ionize the surrounding air. The thin pin acts similarly to the machine sewing needle, also seen in the simulation result. The construction nail performance is closest to our calculated ideal needle shape, mainly because of the diameter. The ideal needle produces the least amount of charges. However, the charges propagate in the needle direction, which is desirable to transfer more momentum in the intended flow direction.

needle body diameter, primarily influenced by tip radius. From here, we will only report results for the $d= 2$ mm body diameter. It consistently yields the best overall airflow velocity magnitude and power consumption performance.

3.3. Ideal needle shape for dielectric configuration

When a dielectric is introduced near the needle, the situation changes. The airspeed becomes highly dependent on the tip radius and angle. Here, we should envisage sharp angles of about 10° to obtain high airflow speeds and efficiently generated airflow, as seen in Fig. 11. For
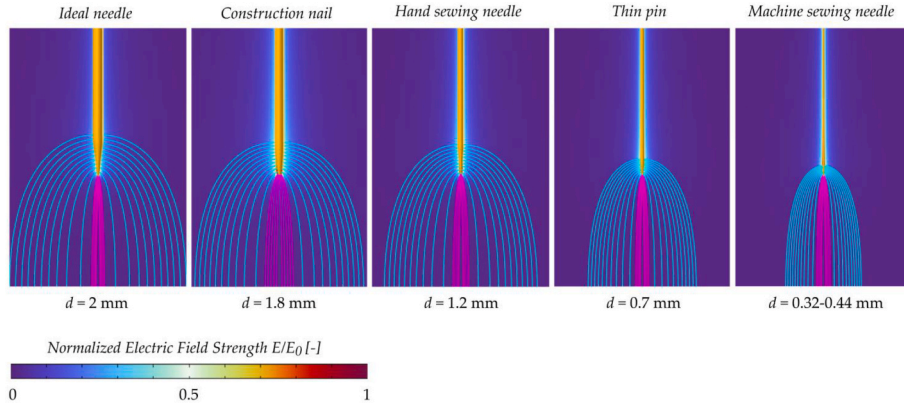
Fig. 10. A comparison of electric field lines for common needle shapes. The comparison illustrates the effect of needle diameter on electric field line direction and dispersion. The magenta-colored field lines represent locations of higher ionization activity. In contrast, the cyan-colored field lines represent needle regions with little to no ionization activity. This comparison shows how different needle types cause asymmetries in the electric field. Electric field asymmetries promote efficient, stable discharge production, which is critical for improving electrohydrodynamic performance.
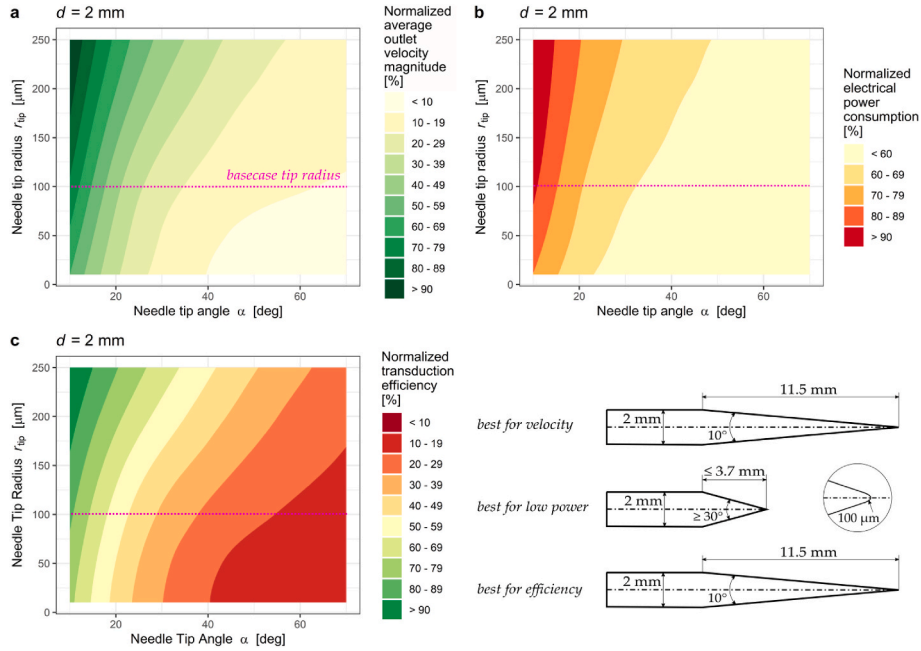
Fig. 11. Normalized velocity, power consumption, and transduction efficiency maps for the configuration involving a nearby dielectric. Compared to the free flow configuration, we can now observe a distinct influence of the needle body parameters on the average outled velocity magnitude. The best-performing needle to obtain more flow has a sharp angle. An angle of 30° or more is beneficial when optimizing for low power.

optimized power consumption, a short conical needle tip with an angle of at least 30° performs better.
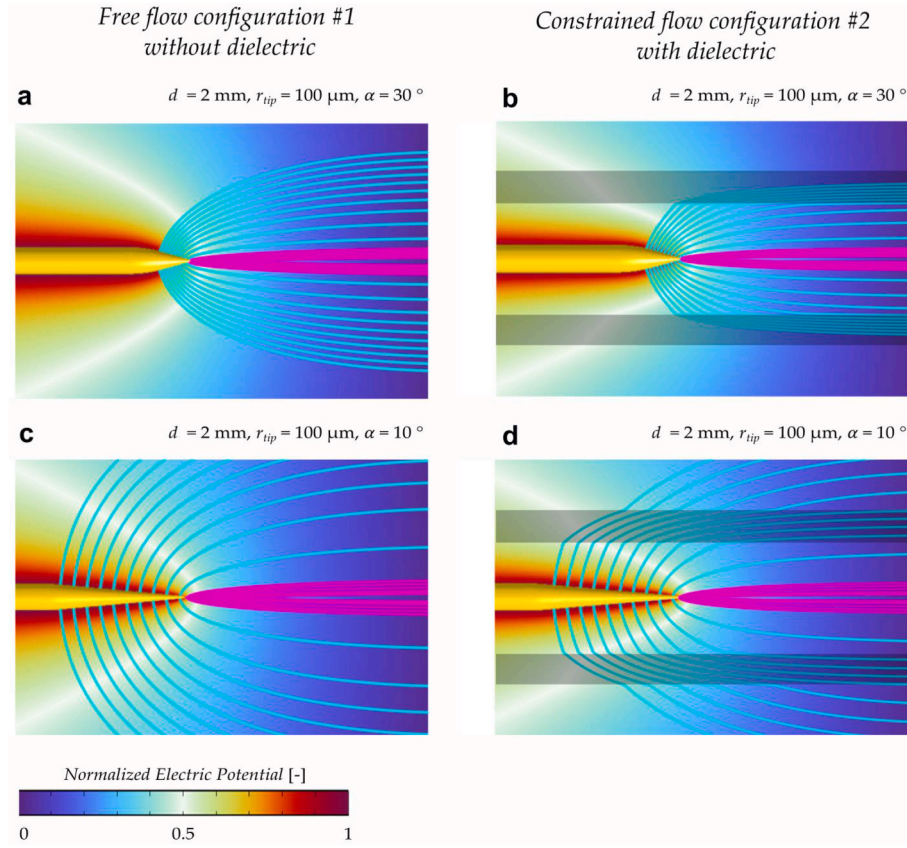
Compared to the free flow configuration, a dielectric causes alterations in the electric field, requiring different needle shapes to tackle the shift in symmetries. This comparison is shown in Fig. 12. The electric field lines are distorted, and regions of high line density appear. That way, the needle may ionize elsewhere than on the tip, acting like the previously seen machine sewing needle. Therefore it is vital to ensure a sustained discharge via sharp angles. We observe in Fig. 11a that the velocity responds sensitively to geometrical changes. This is because the introduction of the dielectric distorts the electric field components such that the electric field lines become dense, as seen in Fig. 12a and b. The field lines indicate the direction of momentum transfer upon which the Coulomb force acts. A more detailed evaluation of charge production and charge directionality is provided in Supplementary Material A. Therefore, we must aspire to reduce the field line density perpendicular to the needle axis. We achieve a reduction by lengthening the needle

cone, as shown by comparing Fig. 12b and d. The direct effect of needle geometry on the airflow is seen in the upper left corner of Fig. 11a, where we note a normalized velocity of >90 %. At the same time, it may drop to less than a tenth in the lower right corner of the map.

We also find an opposite trend in transduction efficiency compared to the free flow case. The tip radius also appears to gain importance seen by the curvature of the isosurfaces according to Fig. 11c compared to Fig. 8c. The ability of the needle to transform electrical energy into kinetic energy can range from over 90 % to less than 10 %, thus completely changing the performance characteristics when a dielectric is introduced. Our ideal needle shape for a configuration involving a dielectric is $d = 2$ mm, $\alpha = 10°$ and $r_{tip} = 100$ μm.

The effect of the needle tip angle on the airflow is demonstrated in Fig. 13. Here, we show flow fields corresponding to various needle tip angles ranging from 10° to 70°. These flow fields show that the needle tip angle significantly impacts the strength and distribution of the generated airflow. Notably, the 10° needle tip angle creates a strong

Fig. 12. Electric potential and electric field lines comparison between free flow configuration #1 without dielectric and constrained flow configuration #2 with dielectric. The field lines starting from the needle tip are magenta colored, while the field lines from the needle cone are cyan. Between Subfigure (a) and (b), we observe that the dielectric strongly contracts the field lines, increasing its density within the material and, as such, the risk of electrical breakdown. We can relax the accumulation of field lines by choosing a 10° cone angle as in Subfigure (c) and (d). Then, the field lines starting from the angle can reach the ground with less contraction and distortion.

airflow, propelling the air jet up to 5 m s^{-1}. A 70° needle tip angle, on the other hand, produces a modest jet that barely exceeds 1 m s^{-1}. This wide range of airflow speeds demonstrates the importance of needle tip geometry in maximizing electrohydrodynamic performance. Our CFD visualizations demonstrate a significant shift in airflow dynamics by changing the needle tip angle. The data shown in Fig. 13 validates the optimal needle shape we propose for dielectric configurations. A needle with a diameter $d = 2 \text{ mm}$, a sharp angle of $\alpha = 10°$ and a tip radius $r_{tip} = 100 \text{ } \mu\text{m}$ maximises the velocity and efficiency of the generated airflow.

3.4. Ideal needle shape under the influence of flow contraction via nozzle geometry

We continue to zone further in the ideal needle shape when a nozzle is added to the dielectric configuration. A nozzle is helpful for aerodynamically finetuning the flow conditions by contraction. It reduces the static pressure and increases the velocity to create a more powerful air jet with more momentum as long as pressure losses do not exceed dynamic pressure. This is interesting in areas where we desire to construct an electrohydrodynamic air blower with higher airspeeds. In Fig. 14, there are six performance maps for transduction efficiency. We compare transduction efficiency as it provides information about airflow and electric power consumption. Additionally, we show the impact of varying the inter-electrode distance δ.

The introduction of the nozzle slightly varies the efficiency regions. We agree that sharp angles ($<20°$) are always preferred for the dielectric and nozzle configurations. Regarding tip radii, the dielectric configuration becomes almost radius-independent with increasing distance

(Fig. 14a–c). This may be rooted in the directionality of charge propagation as detailed in Supplementary Material A; for example, with increased distance between electrodes, the charges produced on the electrode find more space to propagate and exchange momentum. For shorter distances, they would deposit on the ground sooner. With the dielectric nozzle configuration, we find that sharp angles ($< 20°$) and a strong curvature ($< 100 \text{ } \mu\text{m}$) are beneficial, see Fig. 14f.

When introducing the nozzle with the ambition to increase the airflow jet's strength, we also need to consider the size of the nozzle gap. Fig. 15 shows the normalized transduction efficiency for the previously mentioned ideal needle shape for various squared nozzle contraction ratios. We find an optimum at a contraction ratio of 0.5, corresponding to a gap size of $\varepsilon = 3.5 \text{ mm}$. In practice, one would design an electrohydrodynamic air-jet generator with a nozzle size of 2ε as this simulation is conceived on a 2D-axisymmetric configuration. Compared to the basecase situation, the wider gap size increases the transduction efficiency from approximately 75 %–100 %. In this case, we simultaneously have an electrostatic and aerodynamic improvement as the shifting of the ground has implications on the electric field lines and the flow contraction.

3.5. Optimum operation conditions for the ideal needle shape in the nozzle configuration

The configuration with dielectric and nozzle has interesting application possibilities when designing small air blowers. Fig. 16 shows the performance maps of the proposed ideal needle when the voltage is variable. Our needle with a sharp tip angle of 10° performs most efficiently at an operating voltage between 6 and 25 kV. As expected, the
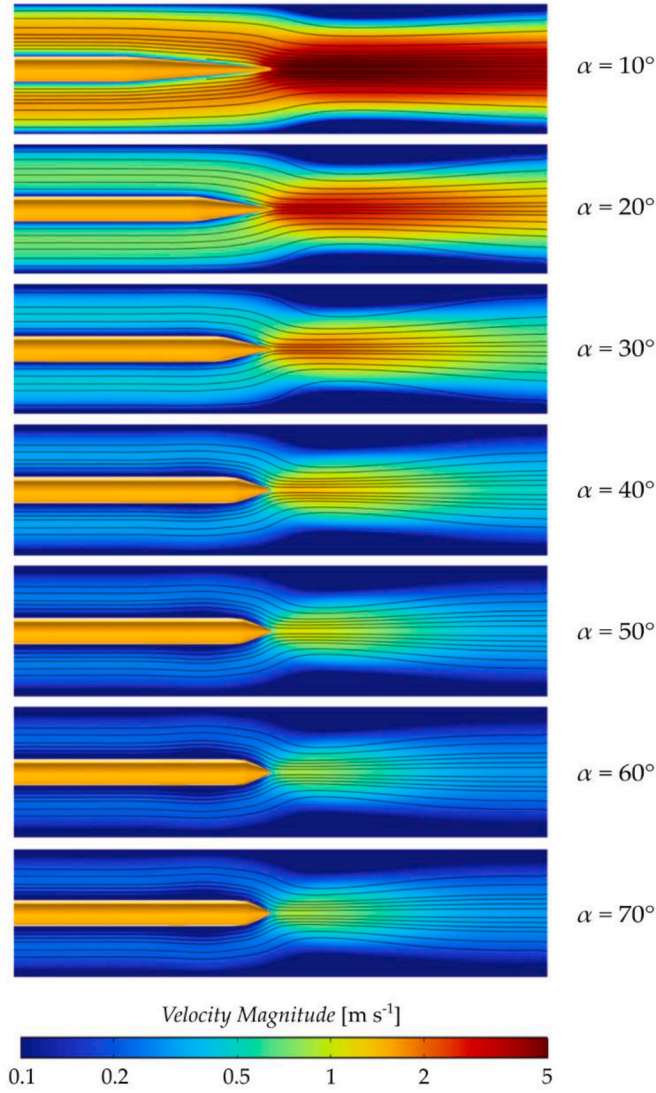
Fig. 13. Comparison of CFD flow fields in logarithmic color scale for needle tip angles ranging from 10 to 70°. These graphics show how the needle tip shape affects the strength and distribution of the generated airflow. The results show that a sharper needle tip angle (10°) promotes stronger airflow up to 5 m s^{-1}. In contrast, a broader angle of 70° generates weaker airflow, just around 1 m s^{-1}.

highest velocities and power consumption are achieved at the highest voltages. However, in practice, such high voltages may cause a breakdown. Breakdown occurs when the local field strength is too high to sustain a continuous discharge, and the discharge switches to an uncontrolled arc discharge. A value of 20 kV or less appears to be an ideal setting for operating the proposed 10° needle in an energy-efficient way based on the transduction efficiency map in Fig. 16c. Interestingly, as for the transduction efficiency, a sink region forms for angles between 55° and 65° and between 15 and 18 kV. It is not discernible which complex mechanics involved in the discharge and momentum transfer processes are responsible.

4. Discussion

We have proposed optimal needle shapes for three different configurations: free flow (#1), constrained flow with a dielectric (#2), and when a nozzle is added to the dielectric (#3). Our design space considered parameters like the needle tip radius, the needle tip angle, the needle body diameter, the needle-collector distance, the operating voltage, and the nozzle gap size. This extensive parametrization provides a comprehensive understanding of the ideal needle shape for EHD-driven flows for various application scenarios.

For manufacturing simplicity, we endorse a tip radius of $r_{tip} = 100\,\mu$m. Our findings reveal that blunt needles offer superior energy consumption and air flow strength performance in a free-flow context, possibly due to the generous spacing between electric field lines. On the other hand, in constrained flow situations, sharp needles emerged as the optimal choice, offering enhanced airflow and lower energy consumption. In this case, a larger conical tip increases the space between the electric field lines, enhancing the flow characteristics along the needle axis direction.

This study plays a crucial role in maximizing the efficiency of EHD generators, demonstrating that simply adjusting the needle geometry can yield significant electrostatic and aerodynamic improvements. Our study aimed to design a needle capable of creating a strong airflow jet for application in EHD air amplifiers [33], a new noiseless, low-energy fan category. These EHD air amplifiers, or ionic wind amplifiers, amplify an EHD airstream via air entrainment on a Coanda surface, where a strong ionic wind jet is crucial. Further potential applications for the optimized needle are scenarios where the emitter-collector arrangement is encased in a dielectric environment, like in (miniaturized) electronic cooling applications [34,35].

Our study does not, however, lack limitations. Due to our reliance on a two-dimensional axisymmetric model, we could not evaluate the performance of multiple needles on various axes or determine which needle shape would be most effective in a needle array configuration. From a research standpoint, dielectric simulations could be expanded to evaluate a broader spectrum of materials with varying dielectric constants, thicknesses, and dielectric-needle distances.

This study employs a complex modeling strategy as an essential tool for rapidly optimizing EHD air movers. Rather than refining needle emitters solely for velocity and energy consumption, our method could also be used to find needle shapes optimized for pressure-rise-related applications. Our model enables us to investigate the effect of needle geometries on pressure reductions and fluid velocities, two significant obstacles to the development of EHD technologies. By utilizing this technique, we can advance our knowledge and development of EHD systems by identifying optimal needle shapes that increase the velocity of the generated airflow and effectively manage pressure drops, thereby optimizing the energy efficiency of such devices.

Despite its practicality, our model could benefit from further refinement. Fig. 2b depicts an unanticipated result regarding power consumption, particularly for the free flow configuration. A decrease in the radius of curvature is generally expected to increase electric current and power consumption. However, our simulations predict a slight decrease in energy consumption. This divergence highlights the complex interplay of factors in electrohydrodynamic airflow and the need to advance theoretical models to comprehend these phenomena for needle electrodes completely. Reconsidering the Peek-Kaptzov ionization condition could yield valuable insights for interpreting these observations.

5. Conclusion

This comprehensive simulations study provided valuable insights on the ideal needle shape for three configurations of EHD-powered airflow generators: a single needle in an open space, including a dielectric, and adding a nozzle. The design space of various needle parameters was explored with a fully coupled and validated EHD model in a 2D axisymmetric setup. Our rigorous parametric analyses have helped determine the best needle shapes to use in various scenarios and show the profound effect of needle geometry on the efficacy and performance of EHD devices. Our study has contributed the following key innovations and scientific findings:

- Doubling the airflow velocity with geometry alterations only: In dielectric enclosures, the optimal needle shape has a body diameter
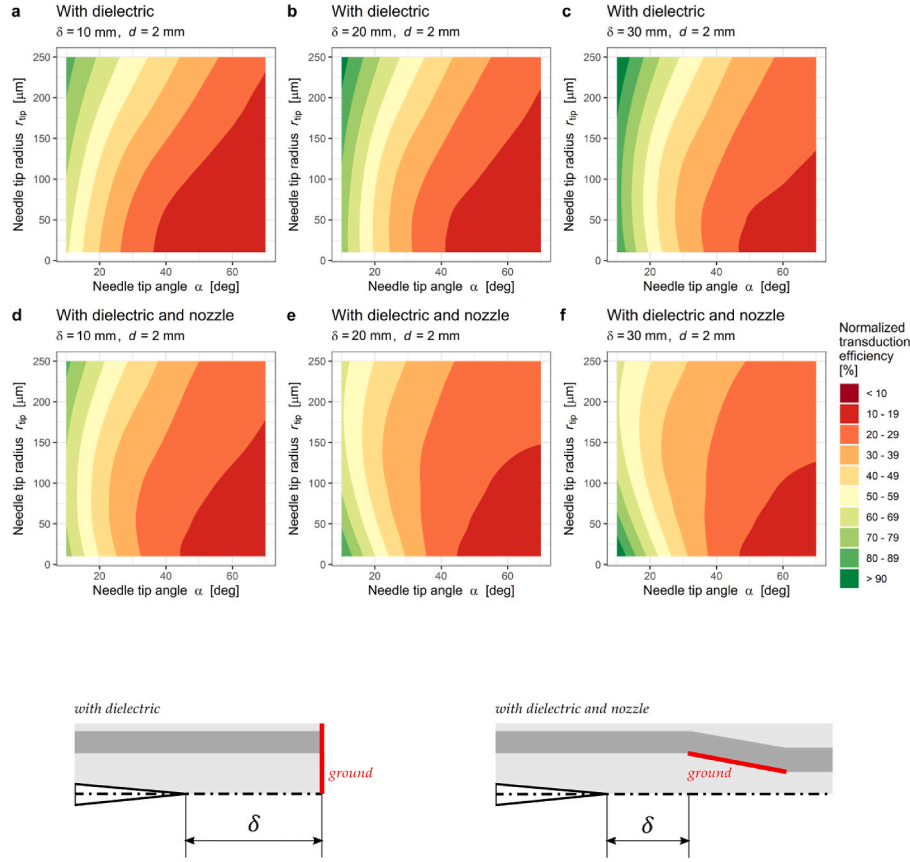
Fig. 14. Normalized transduction efficiency maps comparing the dielectric-only configuration to the dielectric and nozzle configuration. In addition, we compare how the distance between the needle and the ground influences the map. The best efficiencies in the dielectric configuration are reached at sharp angles and larger tip radii (upper left corner, a-c). When a nozzle is introduced, the efficiency map shifts, and we obtain the best results towards smaller radii. Overall we can state that with increasing distance, a larger tip curvature (250 *μm*) is preferable, while in a nozzle configuration, the tip curvature should be kept as little as possible (10 *μm*).
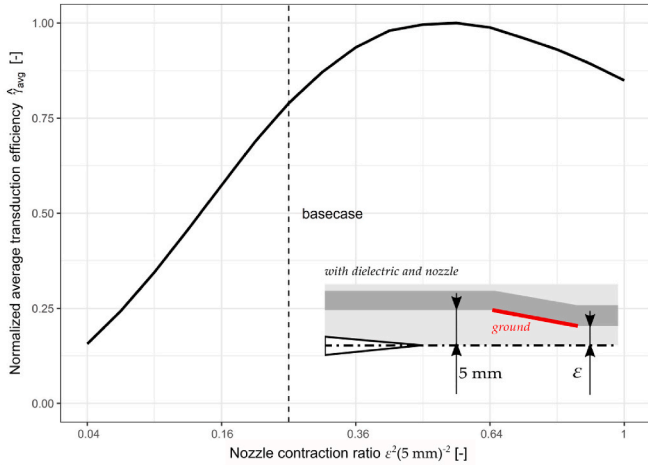

Fig. 15. Transduction efficiency depends on the nozzle gap size for the nozzle configuration. The needle has dimensions of $d = 2\,mm$, $\alpha = 10°$ and $r_{tip} = 100\,μm$. We find a maximum plateauing around a contraction ratio of 0.5, corresponding to a gap size $\varepsilon = 3.5\,mm$. The nozzle contraction ratio is squared based on the ratio of areas before and after the nozzle in this 2D-axisymmetric configuration.

of 2 mm, a needle tip radius of 100 μm, and a needle tip angle of 10°. It can double the average airflow velocity while only increasing energy consumption by 20 %, significantly enhancing EHD devices' performance.

- Energy consumption optimization: We found that careful needle design can effectively optimize energy consumption. For instance, the optimal free-flow needle shape has a body diameter of 2 mm, a needle tip radius of 100 μm, and a needle tip angle of $\geq 30°$. Compared to the benchmark, it consumes at least 30 % less power while retaining its aerodynamic performance.

- Informed design parameter selection: Our extensive parametric results show that needle design parameters substantially impact EHD device performance. We created performance maps to help with the needle engineering process. For example, using a needle with a 2 mm body diameter can cut power usage by 75% compared to a pin-like needle with a 0.44 mm diameter, highlighting the critical significance of needle geometry in enhancing energy efficiency.

- Unveiling geometry-ionization interactions: Our study is the first to investigate how the intricate geometry of a needle impacts asymmetries in the electric field, which in turn affects ionization efficacy and momentum exchange. Adding a flow contraction geometry to the EHD system, for example, causes a shift in the performance map, and the most efficient ionization voltage is 20 kV.

- Optimal nozzle gap size: Our findings indicate that 7 mm is the optimal spacing size for airflow contraction in nozzle devices. Deviations from this dimension, such as our base case with a 5 mm nozzle gap, resulted in a 25% decrease in transduction efficiency. This highlights the significance of a holistic approach to the design of EHD devices, which goes beyond needle geometry to include surrounding structures and fluid-structure interactions.

The findings reported here highlight the advancements in our understanding and performance of EHD technology. We provided solid
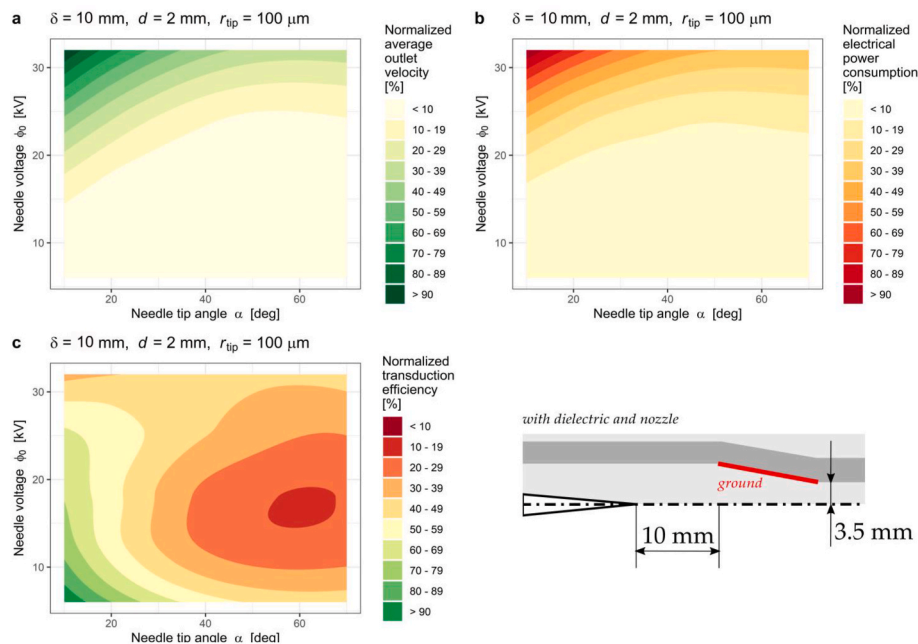
Fig. 16. Performance maps of the ideal needle in the nozzle configuration. The inter-electrode distance δ [mm], the needle body diameter d [mm] and tip radius r_{tip} [μm] remain fixed while the voltage and tip angle are varied. With the highest voltage and lowest tip angles, we achieve the highest airspeeds and power consumption. The transduction efficiency chart also shows a region of very low efficiency. Based on this evaluation, we recommend an operation voltage of $\varphi_0 = 20\,kV$ for electrohydrodynamic air jet generators with a nozzle.

guidelines for designing customized needle shapes in a range of EHD applications, such as thermal heat management, EHD air blowers, and EHD air amplifiers, as a result of this research. While we are confident in our progress, we continue to embrace the dynamic nature of EHD as an emerging technology and look forward to further advances and commercial exploitation.

Author contributions

Donato Rubinetti: Conceptualization, Methodology, Investigation, Project Management, Writing – review, and editing. Kamran Iranshahi: Methodology, Writing – review, and editing. Daniel I. Onwude: Writing – review, and editing. Bart M. Nicolaï;: Writing – review, and editing. Lei Xie: Methodology, Writing – review, and editing. Thijs Defraeye: Conceptualization, Methodology, Supervision, Funding Procurement, Project Management, Writing – review, and editing.

Declaration of competing interest

The authors declare that they have no known competing financial interests or personal relationships that could have appeared to influence the work reported in this paper.

Data availability

Data will be made available on request.

Appendix A. Supplementary data

Supplementary data to this article can be found online at https://doi.org/10.1016/j.elstat.2023.103876.

References

[1] L. Zhao, K. Adamiak, EHD flow in air produced by electric corona discharge in pin–plate configuration, J. Electrost. 63 (3–4) (Mar. 2005) 337–350, https://doi.org/10.1016/J.ELSTAT.2004.06.003.

[2] H. Xu, et al., Flight of an aeroplane with solid-state propulsion, Nat 563 (7732) (Nov. 2018) 532–535, https://doi.org/10.1038/s41586-018-0707-9, 2018 5637732.

[3] J. Zhang, F.C. Lai, Effect of emitting electrode number on the performance of EHD gas pump in a rectangular channel, J. Electrost. 69 (6) (Dec. 2011) 486–493, https://doi.org/10.1016/J.ELSTAT.2011.06.007.

[4] J.H. Sung, M. Kim, Y.J. Kim, B. Han, K.J. Hong, H.J. Kim, Ultrafine particle cleaning performance of an ion spray electrostatic air cleaner emitting zero ozone with diffusion charging by carbon fiber, Build. Environ. 166 (Dec. 2019), 106422, https://doi.org/10.1016/J.BUILDENV.2019.106422.

[5] A.A. Ramadhan, N. Kapur, J.L. Summers, H.M. Thompson, Numerical development of EHD cooling systems for laptop applications, Appl. Therm. Eng. 139 (Jul. 2018) 144–156, https://doi.org/10.1016/j.applthermaleng.2018.04.119.

[6] M. Tanski, et al., A system for cooling electronic elements with an EHD coolant flow, J. Phys. Conf. Ser. 494 (1) (Apr. 2014), 012010, https://doi.org/10.1088/1742-6596/494/1/012010.

[7] H. Moayedi, H. Mohaddes Deylami, Electrohydrodynamic performance improvement using different actuation modes in a channel: a CFD simulation study, Appl. Therm. Eng. 211 (Jul. 2022), 118471, https://doi.org/10.1016/J.APPLTHERMALENG.2022.118471.

[8] E. Moreau, Airflow control by non-thermal plasma actuators, J. Phys. D Appl. Phys. 40 (3) (Jan. 2007) 605, https://doi.org/10.1088/0022-3727/40/3/S01.

[9] M.J. Johnson, D.B. Go, Recent advances in electrohydrodynamic pumps operated by ionic winds: a review, Plasma Sources Sci. Technol. 26 (10) (Oct. 2017), 103002, https://doi.org/10.1088/1361-6595/AA88E7.

[10] M. Rickard, D. Dunn-Rankin, F. Weinberg, F. Carleton, Maximizing ion-driven gas flows, J. Electrost. 64 (6) (Jun. 2006) 368–376, https://doi.org/10.1016/j.elstat.2005.09.005.

[11] A. Martynenko, T. Kudra, Electrically-induced transport phenomena in EHD drying - a review, Trends Food Sci. Technol. 54 (Aug. 01, 2016) 63–73, https://doi.org/10.1016/j.tifs.2016.05.019. Elsevier Ltd.

[12] D. Rubinetti, K. Iranshahi, D. Onwude, B. M. Nicolaï, L. Xie, and T. Defraeye, "Electrohydrodynamic Air Amplifier for Low-Energy Airflow Generation - Experimental Proof-Of-Concept," doi: 10.31224/2508.

[13] I. Bashkir, A. Martynenko, Optimization of multiple-emitter discharge electrode for electrohydrodynamic (EHD) drying, J. Food Eng. 305 (Sep. 2021), 110611, https://doi.org/10.1016/J.JFOODENG.2021.110611.

[14] J.F. Zhang, X.W. Wu, J.G. Qu, D.W. Zhang, Z.G. Qu, Electrohydrodynamic and heat transfer characteristics of a planar ionic wind generator with flat electrodes, Appl. Therm. Eng. 211 (Jul. 2022), 118508, https://doi.org/10.1016/J.APPLTHERMALENG.2022.118508.

[15] N. Monrolin, O. Praud, F. Plouraboué, Electrohydrodynamic ionic wind, force field, and ionic mobility in a positive dc wire-to-cylinders corona discharge in air, Phys. Rev. Fluids 3 (6) (Jun. 2018), https://doi.org/10.1103/PhysRevFluids.3.063701.

[16] E.J. Shaughnessy, G.S. Solomon, Electrohydrodynamic pressure of the point-to-plane corona discharge, Aerosol Sci. Technol. 14 (2) (1991) 193–200, https://doi.org/10.1080/02786829108959482.

[17] M.J. Johnson, R. Tirumala, D.B. Go, Analysis of geometric scaling of miniature, multi-electrode assisted corona discharges for ionic wind generation, J. Electrost. 74 (Apr. 2015) 8–14, https://doi.org/10.1016/J.ELSTAT.2014.12.001.

[18] M. Robinson, Movement of air in the electric wind of the corona discharge, Trans. Am. Inst. Electr. Eng. Part I Commun. Electron. 80 (2) (2013) 143–150, https://doi.org/10.1109/tce.1961.6373091.

[19] S. Kanazawa, W. Imagawa, S. Matsunari, S. Akamine, R. Ichiki, K. Kanazawa, Ionic wind devices prepared by a 3D printer, Oct. 14, 2021. [Online], https://ijpest.securesite.jp/Contents/11/1/PDF/11-01-038.pdf.

[20] D. Rubinetti, K. Iranshashi, D. Onwude, L. Xie, B. Nicolai, and T. Defraeye, "An In-Silico Proof-Of-Concept of Electrohydrodynamic Air Amplifier for Low-Energy Airflow Generation," doi: 10.31224/2436.

[21] F.C. Lai, EHD gas pumping – a concise review of recent development, J. Electrost. 106 (Jul. 2020), 103469, https://doi.org/10.1016/J.ELSTAT.2020.103469.

[22] A. Kasdi, Experimental and Numerical Modeling of Corona Discharge Generated in an Electrostatic Precipitator, Jan. 2019, https://doi.org/10.1109/CISTEM.2018.8613435.

[23] T. Defraeye, A. Martynenko, Electrohydrodynamic drying of food: new insights from conjugate modeling, J. Clean. Prod. 198 (2018) 269–284, https://doi.org/10.1016/j.jclepro.2018.06.250.

[24] D.I. Onwude, K. Iranshahi, D. Rubinetti, A. Martynenko, T. Defraeye, Scaling-up electrohydrodynamic drying for energy-efficient food drying via physics-based simulations, J. Clean. Prod. 329 (Dec. 2021), 129690, https://doi.org/10.1016/J.JCLEPRO.2021.129690.

[25] B. Behzadnezhad, B.D. Collick, N. Behdad, A.B. McMillan, Dielectric properties of 3D-printed materials for anatomy specific 3D-printed MRI coils, J. Magn. Reson. 289 (Apr. 2018) 113, https://doi.org/10.1016/J.JMR.2018.02.013.

[26] K. Iranshahi, A. Martynenko, T. Defraeye, Cutting-down the energy consumption of electrohydrodynamic drying by optimizing mesh collector electrode, Energy 208 (Oct. 2020), 118168, https://doi.org/10.1016/j.energy.2020.118168.

[27] T. Defraeye, A. Martynenko, Electrohydrodynamic drying of food: new insights from conjugate modeling, J. Clean. Prod. 198 (Oct. 2018) 269–284, https://doi.org/10.1016/j.jclepro.2018.06.250.

[28] Y. Guan, R.S. Vaddi, A. Aliseda, I. Novosselov, Analytical model of electro-hydrodynamic flow in corona discharge, Phys. Plasmas 25 (8) (Aug. 2018), https://doi.org/10.1063/1.5029403.

[29] K. Adamiak, P. Atten, Simulation of corona discharge in point–plane configuration, J. Electrost. 61 (2) (Jun. 2004) 85–98, https://doi.org/10.1016/J.ELSTAT.2004.01.021.

[30] H.M. Deylami, N. Amanifard, F. Dolati, R. Kouhikamali, K. Mostajiri, Numerical investigation of using various electrode arrangements for amplifying the EHD enhanced heat transfer in a smooth channel, J. Electrost. 71 (4) (Aug. 2013) 656–665, https://doi.org/10.1016/J.ELSTAT.2013.03.007.

[31] E.D. Fylladitakis, A.X. Moronis, K. Kiousis, Design of a prototype EHD air pump for electronic chip cooling applications, Plasma Sci. Technol. 16 (5) (May 2014) 491, https://doi.org/10.1088/1009-0630/16/5/09.

[32] S. Wang, J.G. Qu, L.J. Kong, J.F. Zhang, Z.G. Qu, Numerical and experimental study of heat-transfer characteristics of needle-to-ring-type ionic wind generator for heated-plate cooling, Int. J. Therm. Sci. 139 (May 2019) 176–185, https://doi.org/10.1016/J.IJTHERMALSCI.2019.01.032.

[33] D. Rubinetti, K. Iranshahi, D. Onwude, B. Nicolaï, L. Xie, T. Defraeye, Electrohydrodynamic air amplifier for low-energy airflow generation—an experimental proof-of-concept, Front. Energy Effic. 1 (1) (Mar. 2023), https://doi.org/10.3389/FENEF.2023.1140586.

[34] J. Darabi, M.M. Ohadi, D. DeVoe, An electrohydrodynamic polarization micropump for electronic cooling, J. Microelectromech. Syst. 10 (1) (Mar. 2001) 98–106, https://doi.org/10.1109/84.911097.

[35] H.C. Wang, N.E. Jewell-Larsen, A.V. Mamishev, Thermal management of microelectronics with electrostatic fluid accelerators, Appl. Therm. Eng. 51 (1–2) (Mar. 01, 2013) 190–211, https://doi.org/10.1016/j.applthermaleng.2012.08.068. Pergamon.